Evaluation of Knee Implant Alignment using Radon Transformation

Guillaume Pascal[1], Andreas Møgelmose[1] and Andreas Kappel[2,3]
[1] *Visual Analysis of People Laboratory, Aalborg University, Denmark*
[2] *Department of Clinical Medicine, Aalborg University, Denmark*
[3] *Interdisciplinary Orthopaedics, Aalborg University Hospital, Denmark*

Keywords: Radiograph, Total Knee Arthroplasty, Medical Image Processing.

Abstract: In this paper we present a method for automatically computing the angles between bones and implants after a knee replacement surgery (Total Knee Arthroplasty, TKA), along with the world's first public dataset of TKA radiographs, complete with ground truth angle annotations. We use the Radon transform to determine the angles of the relevant bones and implants, and obtain 94.9% measurements within 2°. This beats the current state-of-the-art by 2.9%. The system is thus ready to be used in assisting surgeons and replacing time consuming and observer dependent manual measurements.

1 INTRODUCTION

Knee osteoarthritis is a common cause of pain and disability, primarily in the elderly population (Hunter and Bierma-Zeinstra, 2019). In end-stage knee osteoarthritis, surgical treatment with total knee arthroplasty (TKA) is proven effective both in relieving pain and restoring function (Price et al., 2018). Longevity of the implant, pain relief, and functional outcome following TKA surgery are all dependent on the surgeon's ability to reconstruct the joint by addressing both implant alignment and soft-tissue stability (Gromov et al., 2014; Kappel et al., 2019).

Knee alignment is judged by both clinical examination and radiographs prior to the TKA operation, and anatomical variations relevant for the procedure are observed. During surgery, the bone cuts that will determine TKA alignment are typically performed with the aid of mechanical instruments, though adjustments are made based on both the preoperative examination and the direct observation of bony and other anatomical landmarks. TKA alignment is therefore influenced by both individual anatomical variations and by surgeon experience and preference. Because of this, variations from optimal alignment can be observed. Routine postoperative knee radiographs deliver feedback to the surgical team, visualizing implant fixation, sizing, placement and alignment. The Knee Society has defined standardized methods to measure implant fixation and alignment from short films (Meneghini et al., 2015). These measurements, however, are time-consuming and might be observer dependent. In our experience most institutions and individual surgeons rely only on radiographs for non-systematic visual feedback.

We believe that routine standardized analysis of postoperative radiographs would deliver valuable information to both individual surgeons and institutions and thereby further optimize the surgical outcomes. The aim of this work was to develop a method allowing fast, standardized, observer independent feedback on coronal alignment measurement following TKA by automation of the measurements.

In layman's terms, the purpose of the system presented in this paper is to use a radiograph of a knee to determine the angle between the anatomic axis of the femur and the most distal part of the femoral implant, as wells as the angle between the anatomic axis of the tibia and the tibial tray. Jump ahead to fig. 14 for a visualization of this.

2 RELATED WORK

Automated analysis of knee radiographs has been an active research area for more than two decades. There was a flurry of activity in the late 90s, starting with attempts to measure the kinematics of knees using a sequence of X-ray fluoroscopic images by comparing a silhouette of the prosthesis to silhouettes on the images (Banks and Hodge, 1996). Similar work using edges of implants was also presented with the use case

Pascal, G., Møgelmose, A. and Kappel, A.
Evaluation of Knee Implant Alignment using Radon Transformation.
DOI: 10.5220/0010192405870594
In *Proceedings of the 16th International Joint Conference on Computer Vision, Imaging and Computer Graphics Theory and Applications (VISIGRAPP 2021) - Volume 4: VISAPP*, pages 587-594
ISBN: 978-989-758-488-6
Copyright © 2021 by SCITEPRESS – Science and Technology Publications, Lda. All rights reserved

of measuring wear on the polyethylene in the implant (Fukuoka et al., 1997, 1999). Others elected to use template matching on a library of prosthesis templates (Hoff et al., 1996, 1998; Walker et al., 1996). Later, a different method more capable of handling occlusions was proposed (Zuffi et al., 1999). An improved model-based method for markerless tracking of implant micromotion has also been presented (Kaptein et al., 2003).

Apart from looking at implants, a number of papers on 3D reconstruction of bones have been presented lately (Baka et al., 2011; Fotsin et al., 2019; Kim et al., 2019; Kasten et al., 2020). For a general overview of work in this vein, a review has also been published (Markelj et al., 2012).

While a number of the aforementioned papers work with knee joints and knee implants, none of them do the post-surgical angle analysis we do in this paper. As far as we know, only one other paper tackles this problem directly (Kulkongkoon et al., 2018). They propose a method based on a multiscale dual filter used to enhance bones followed by a Canny edge detection. A linear regression model is used to compute the bones orientation from control points while the edges of the implants are used to compute their orientation. This method obtained a 92% acceptance rate on a dataset of 91 X-ray images: the difference between the proposed algorithm and the manual evaluation is two degrees or less. The failures occured with patients who had multiple knee replacement surgeries, and images where the two implants are overlapping.

The dataset used for the test by Kulkongkoon et al. (2018) is unfortunately not publicly available, and we are thus unable to directly compare our performance with theirs. Because of this, we do not only propose a new and different angle estimation method, we also present a public dataset of TKA radiographs available for anybody who would like to benchmark their system against ours.

3 DATASET

The dataset used to build and evaluate the proposed method is composed of 137 radiographs of knees from the AP view. Each radiograph is a grayscale image where both implants and bones are displayed by bright pixels, while the background and tissues are darker. The set contains radiographs of both right and left knees with different types of implants. Each image is provided with manually labeled ground truths, as determined by the mean measurements of two surgeons doing a manual evaluation of both tibial and femoral angles. Having two surgeons in the process should reduce observer bias. Histograms of the ground truth angle distributions for both bones are shown in fig. 1. The AAU-TKA dataset is freely available at http://vap.aau.dk/tka.

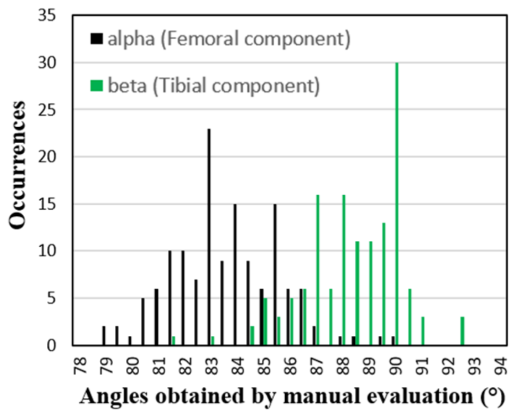

Figure 1: Histogram of the ground truth angle distributions for both femoral and tibial component (alpha in black, beta in green).

4 RADON TRANSFORMATION

The Radon transformation is a crucial part of the proposed solution, and hence we briefly describe it before going into detail about the entire system. We apply the Radon transform to highlight straight lines of images. It is defined in equation (1) for a continuous two dimensional function, or in equation (2) for a discrete two dimensional function (Toft, 1996). The output of the radon transformation is an image called a sinogram. A straight line in the image can be approximated in the corresponding sinogram by a point, whose position depends on the line position and the orientation.

$$S(\theta,\tau) = \int_{-\infty}^{+\infty} I(x, \theta x + \tau)dx \qquad (1)$$

$$S(\theta_k,\tau_h) = \Delta x \sum_{m=0}^{M-1} I(x_m, \theta_k x_m + \tau_h) \qquad (2)$$

In equation (1) S is the sinogram and I the input image. θ and τ represent the slope and the offset of the line. In equation (2) $x_m, m \in [0, M-1]$, θ_k and τ_k are the sampled x, θ and τ and Δx is the sampling distance of x.

5 THE PROPOSED METHOD

The method works in three stages:

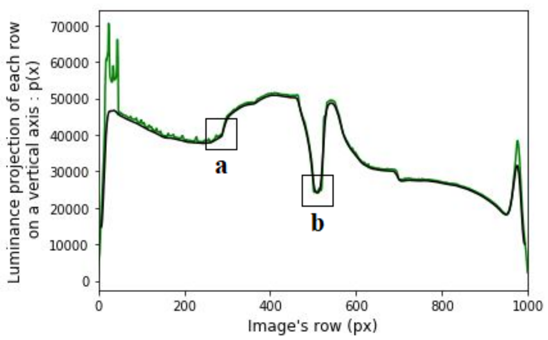

Figure 2: Luminance projection $p(x)$ of the image on a vertical axis (green). Smoothed luminance projection (black). The shape of the implants is visible from pixels 300 to 700, allowing to find (a) the top of the top-implant and (b) the middle of the articulation.

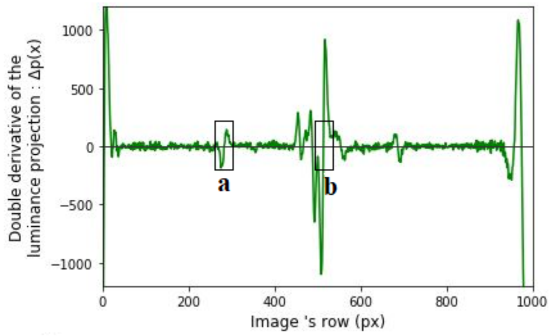

Figure 3: Double derivative $\Delta p(x)$ of the luminance projection displayed on Figure (2). The markers (a) on (b) corresponds to the zero crossing of the corresponding markers on Figure (2).

Image Splitting: Divide the radiograph into three parts: The implant, the femur, and the tibia.

Implant Orientation Estimation: Compute the orientations of the two implant halves.

Bone Orientation Estimation: Compute the orientation of the femur and the tibia.

In the following sections, each of these are described in detail.

5.1 Image Splitting

Dividing the image will enable the system to focus on each of the parts of the radiograph separately during the following steps. The desired split looks like this:

- Implant section: The middle of the image, bounded by a frame, will be used to find the orientation of the two implants
- Femur section: The top of the image, above the frame, will be used to compute the femur orientation
- Tibia section: The bottom of the image, below the frame, will concern the tibia orientation. It also contains the fibula, which is of no interest to us, but complicates the computation slightly.

In the following paragraphs, the top left pixel is defined as the (0,0) coordinate. The x-axis corresponds to the vertical while the y-axis corresponds to the horizontal.

The method must first find the center of the image, defined as the middle of the articulation, and a size of the implant section, determined by the size of the top-implant. In short, we want to find the point (x_0, y_0) in the center between the implants, and the coordinates x_{top} and x_{bottom} defining the top and bottom of the implant section.

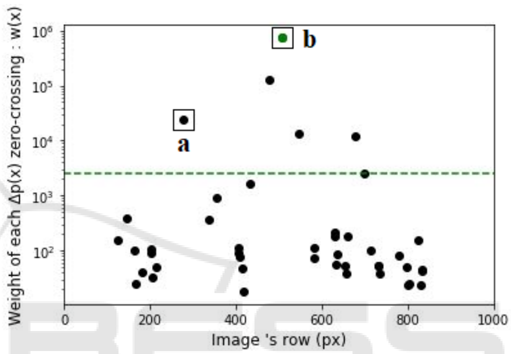

Figure 4: Weight of each zero crossing of the curve in Figure (3). Points above the dashed green line corresponds to the sharpest zero-crossings: (a) is the top of the top-implant and (b) the middle of the articulation.

To achieve this, the program calculates the luminance projection of the image on a vertical axis $p(x)$. Fig. 2 shows a luminance projection $p(x)$, where we can recognize the shape of the two implants. To accurately locate the center and the top of the implant, the double derivative $\Delta p(x)$ is computed as shown on equation 3 below, with output displayed on fig. 3.

$$\Delta p(x) = \frac{d^2}{dx^2}\left[\sum_{y=0}^{m-1} I_{mb}(x,y)\right] \tag{3}$$

$I_{mb}(x,y)$ is the initial $n \times m$ image successively filtered by a median filter and a Gaussian blur. Using a median filter on the image removes the perturbation of the clips used to close the leg after the surgery. A Gaussian blur is also added, as the double derivative is sensitive to noise.

A weight $w(x)$ is determined for each zero crossing in $\Delta p(x)$ as described in equation 4. This highlights the most sudden changes on the curve of $p(x)$.

$$w(x) = \sum_{i=x-\frac{\tau}{2}}^{x+\frac{\tau}{2}} (\Delta p(i))^2 \quad \forall x \,|\, \Delta p(x) = 0 \tag{4}$$

SCITEPRESS SCIENCE AND TECHNOLOGY PUBLICATIONS

The parameter τ represents the width of the rectangular function used to calculate the weight around each zero crossing. Its value must be significantly lower than the height of the image. Note that $w(x)$ is only defined for x where the double derivative $\Delta p(x)$ is equal to zero. Fig. 4 shows the weights obtained for each zero crossing.

The vertical position of the center of the articulation x_0 (equation 5) corresponds to the zero crossing in $\Delta p(x)$ with the highest weight because it is the most sudden change on the representative curve of $p(x)$, as we can see on fig. 2.

$$x_0 = arg\,\underset{x}{max}(\,w(x)\,) \tag{5}$$

Following the same principle, the program is able to find the top of the implant x_{top}, as it is the zero crossing closest to the top of the image with a weight bigger than a certain threshold s, see eq. 6. s is defined proportional to the maximum value of $w(x)$.

$$x_{top} = min(\{x \,|\, w(x) > s\}) + \varepsilon \quad s \propto max(w(x)) \tag{6}$$

The bottom border x_{bottom} of the frame is then set at the same distance from the center of the articulation as the top border from the center of the articulation (eq. 7). Even if the bottom implant is smaller than the top implant, it remains relevant to do so since the part of the bone close to the articulation is generally too curved to be processed in the next steps. That is why a margin ε is also added to expand the frame.

$$x_{bottom} = x_0 + (x_0 - x_{top}) \tag{7}$$

The final step consists of finding the horizontal position of the center of the articulation y_0. This time, the program computes the luminance projection q(y) of the implant section on an horizontal axis. As shown on eq. 8, the projection $q(y)$ is then convolved with a rectangular function $\Pi(y)$.

$$y_0 = arg\,\underset{y}{max}(\,q(y) * \Pi(y)\,) \tag{8}$$

The size of the rectangular function must be similar to the horizontal width of the implants. Since the implants are brighter than the background of the image, the result is a concave curve with a maximum at the middle of the articulation.

The center of the articulation can now be expressed by (x_0, y_0). Fig. 5 shows the final result of the image splitting, with the center of the articulation marked as a white dot and the white frame surrounds the implants with a small margin.

5.2 Implant Orientation Calculation

The implant section bounded by the frame previously defined is used when determining implant orientations. It contains the two implants. The following method allows finding the orientation of each implant regardless of its type and shape, based on the high luminance difference between the implants and the background visible at the center of the articulation.

The method is illustrated in fig. 6. The Radon transform of the image is computed, producing a sinogram. In this sinogram the vertical axis corresponds to the vertical position of a line in the image, while the horizontal axis corresponds to the rotation a line in the image. We can observe a dark shape in this sinogram corresponding to all straight lines that goes through the gap between the two implants. Focusing on the top and bottom corner of this dark shape allows to get the vertical position and the orientation of the two lines tangent to the implants.

In order to improve the precision of this method, a minimum filter is applied to the implant section to increase the size and the contrast of the gap between the implants, leading to a darker and bigger shape in the sinogram, easier to segment. This operation turns out to be particularly useful in the following cases:

- The top surface of the bottom implant is visible on the radiograph, making its edge hardly distinguishable. An example is given on fig. 7. This case appears when the patient's leg is too flexed. The filter smooths the image and the edge is easier to recognize.
- The clips are disrupting the middle image. The minimum filter simply removes these clips, also visible on fig. 7.
- The two implants are too close to each other or even touching as shown on Figure (8). The minimum filter increases the size of the gap without changing the orientation of the implants.

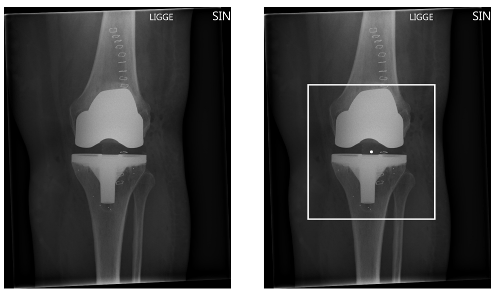

(a) Initial image. (b) Obtained frame.

Figure 5: Example of final result of the image splitting.

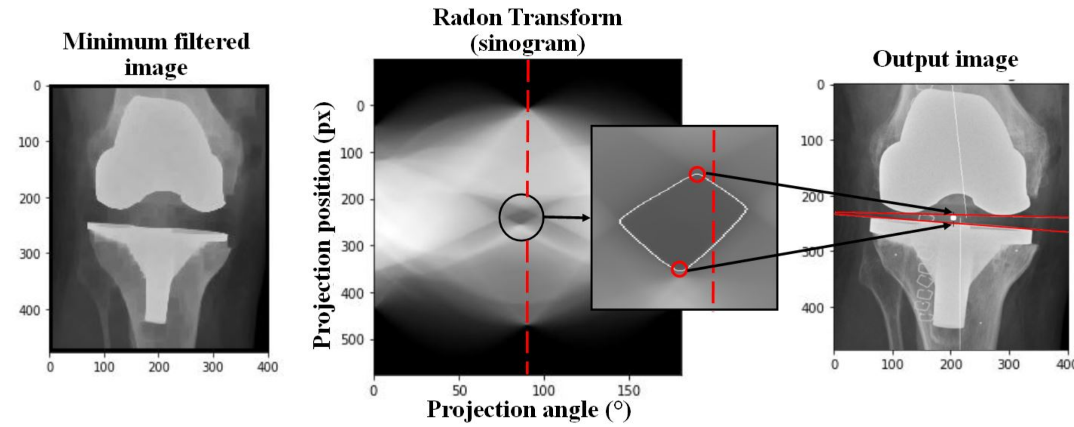

Figure 6: Method for implant orientation calculation. On the left the implant section filtered by a minimum filter is shown. The corresponding sinogram is visible in the middle, with a zoom to its interesting part. The vertical dashed red line corresponds to the 90° projection angle. On the left the resulting lines for each implant are shown.

5.3 Bone Orientation Calculation

The orientation of a bone (femur or tibia) is calculated as the mean of the orientation of its two edges. After applying an edge detector, each edge is approximated with a straight line. It is consequently important to find a way to distinguish the correct edges from the useless ones: the edges of the leg and the fibula interfere with the edges of the femur and the tibia. Thus, approximating the position of the interesting bones is useful.

5.3.1 Approximate Bone Location

In order to locate the bone position, the program computes the luminance projection on an horizontal axis of both top and bottom images. As when finding the horizontal center of the articulation, the projections are convolved by a rectangular function of size similar to the width of the bones. The approximate center of each bone finally corresponds to the maximum of each resulting curve.

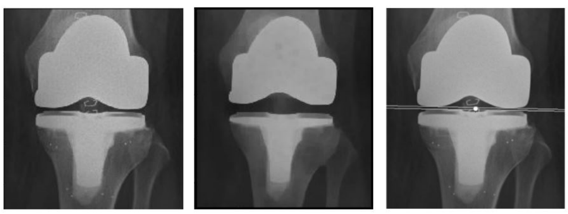

Figure 7: From left to right: Initial image, minimum filtered image, resulting image. Example of radiograph processing with flexed leg, leading to a visible top of the bottom implant.

5.3.2 Edge Detection

A median filter removes the clips and the noise from the initial image. Note that the use of a median filter changes the shape of corners, but the edges of the bones remain unaltered. The obtained image is called I_{med}.

We find the edges as shown on eq. 9. The output image I_{edges} is equal to the difference between the 2D maximum filtered and the 2D minimum filtered image. Note that this image is not binary but shows the magnitude of each edge.

$$I_{edges} = max2D(I_{med}) - min2D(I_{med}) \tag{9}$$

The kernel used is chosen according to the size of the image, and big enough to obtain wide edges so that even sloped bones can be considered and processed. Sloped edges are then approximated with a straight line.

5.3.3 Edge Orientation

The radon transform is applied on both the femur and tibia section of I_{edges}. The edges of the tibia section is visible on fig. 10. The obtained sinogram on fig.

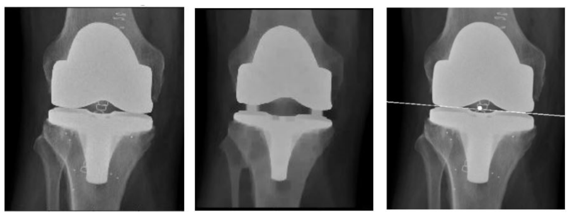

Figure 8: From left to right: Initial image, minimum filtered image, resulting image. Example of radiograph processing with top and bottom implants overlapping.

SCITEPRESS SCIENCE AND TECHNOLOGY PUBLICATIONS

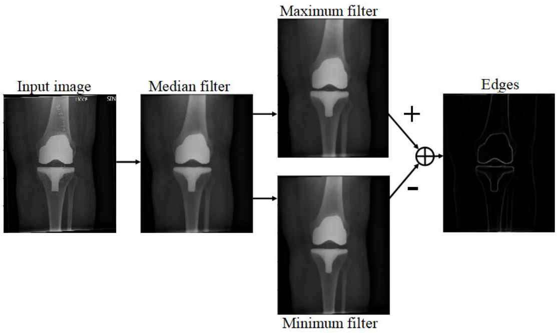

Figure 9: Edge detection method: After a median filter, the maximum and the minimum filtered images are computed. The image of the resulting edges corresponds to the difference between the maximum and the minimum images.

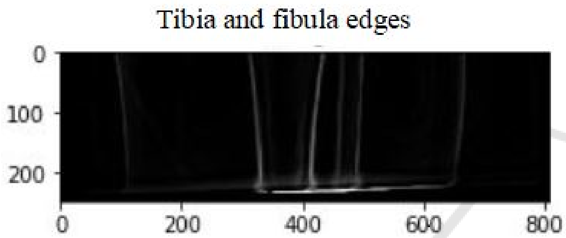

Figure 10: Edges of the tibia section. The tibia and the fibula are visible, as well as faint lines showing the outline of the leg.

11 contains in its center local maximums corresponding to the most significant straight lines. These are the edges of the leg, the tibia and the fibula. The program only keeps the lines corresponding to the two closest maximums on each side of the known approximate location of the bone (see section 5.3.1). Doing so allows to get rid of the leg and fibula perturbation, as their maximums in the sinogram are further away.

In order to find the two closest maximums, the maximum of each row on the sinogram is computed, resulting in a one dimensional representative curve (fig. 12) of the strongest line for each position, independently from their orientation. A peak detection is then computed as follows: a peak is considered as such if it is a local maximum considering the nearest points. To avoid detecting a wrong one, a threshold is set based on the intensity at the known approximate middle of the bone. Finally, the two closest peaks from the approximate middle of the bone are kept. The vertical and horizontal position of these two peaks in the sinogram describes the location and the orientation of each edge of the bone.

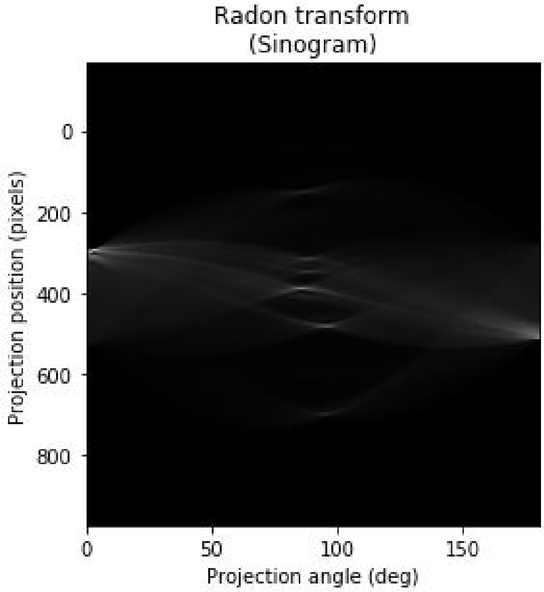

Figure 11: Sinogram of the tibia section edges in fig. 10. Only the center part is kept to get the orientation of the vertical lines (around a projection angle of 90°) corresponding to the bone edges.

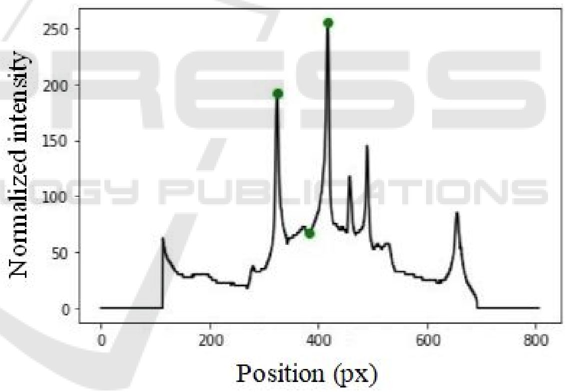

Figure 12: Maximum intensity of each row of the sinogram, showing the strongest edges in fig. 10 independent of the orientation of the lines. The green dots from left to right corresponds to the left edge of tibia (local maximum), the approximate center of the tibia (computed previously) and the right edge of the tibia (local maximum).

6 RESULTS

In this section we evaluate the performance of the system. We compare the output angles with those computed manually by a surgeon. However, we know that the manual approach is observer dependent, so in a separate test, we ask a surgeon to rate the output lines of the system whether they follow the bones and implants with sufficient accuracy.

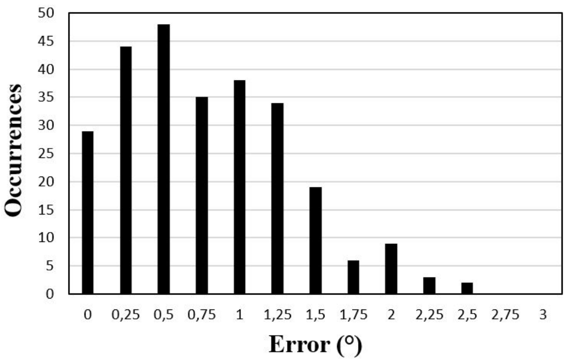

Figure 13: Error distribution on a set of 268 angles. The error is established from the difference between manual and automatic evaluation.

6.1 Comparison between Manual and Computed Angles

Fig. 13 shows the error distribution of 268 computed angles from the set of 137 images (note that 3 images were not processed by the program). The error is defined as the absolute difference between manual results and output angles. As shown in table 1, 94.9% of the angles are within 2° from the manual evaluation. This is generally considered acceptable, and is also the threshold used by Kulkongkoon et al. (2018). At 94.9% we outperform their method by 2.9%, though we are testing on a different dataset, so the results are not directly comparable. Note that the evaluation contains potential human measurement errors as well as rounding errors on the manual measurements, since those angles are rounded to the nearest degree. The ground truth angles have been determined as the mean of two evaluations made by experts in order to reduce observer bias.

Table 1: Proportion of angles under a certain error value.

Error(°)	≤ 0.5	≤ 1.0	≤ 1.5	≤ 2.0
Proportion of angles (%)	43.8	70.3	89.5	94.9

6.2 Evaluation of Output Images by Experts

In our second test, the output images from the program were evaluated by experts. An example is shown on fig. 14. A check was made regarding the correct placement of the different lines displayed: each edge of the tibia and the femur are approximated by a white line, as well as the resulting anatomical axis of each bone. The orientation of each implant is also represented by a tangent line. With a quick visual control, it is simple to observe any error in the program. The output images containing the different lines of the process has been evaluated by experts giving 126/137 (92.0%) accepted cases.

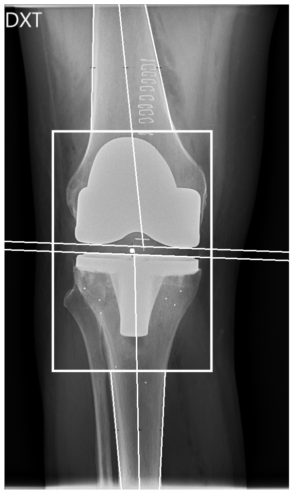

Figure 14: Output image of the program: The white lines giving the orientation of the two implants are visible, as well as the frame bounding them. Each bone edge and shaft is also approximated by a white line.

The errors are mostly due to curved bones, wrong approximation of bones position or images with exceptionally poor contrast.

It is worth noting that this system is intended to be used to assist the surgeon and replace their time consuming manual measurements. As such it is not necessarily a problem if the program fails in a few cases, as the surgeon would be able to determine it from a quick glance at the output image and proceed with manual measurements if the image quality allows it.

7 CONCLUSION

In this paper, a program is presented which automates the control of radiographs following a total knee arthroplasty. The input radiograph is split into three parts corresponding to the femur, the implant, and the tibia, and the orientations of each of these are computed using the Radon transform. Along with this paper, we publish our dataset with corresponding ground truth, so other may improve on our performance. When comparing with the ground truth, 94.9% of the measurements are within 2°, outperforming the state of the art by 2.9%. The method works with a large variety of implant shapes, and displays an output image which simple to verify by the surgeon. The proposed method is a stable and well-defined way to process the images, removing any observer bias which may be present when using manual measurement.

REFERENCES

Baka, N., Kaptein, B. L., de Bruijne, M., van Walsum, T., Giphart, J., Niessen, W. J., and Lelieveldt, B. P. (2011). 2d–3d shape reconstruction of the distal femur from stereo x-ray imaging using statistical shape models. *Medical image analysis*, 15(6):840–850.

Banks, S. A. and Hodge, W. A. (1996). Accurate measurement of three-dimensional knee replacement kinematics using single-plane fluoroscopy. 43:638–649.

Fotsin, T. J. T., Vázquez, C., Cresson, T., and De Guise, J. (2019). Shape, pose and density statistical model for 3d reconstruction of articulated structures from x-ray images. In *2019 41st Annual International Conference of the IEEE Engineering in Medicine and Biology Society (EMBC)*, pages 2748–2751. IEEE.

Fukuoka, Y., Hoshino, A., and Ishida, A. (1997). Accurate 3d pose estimation method for polyethylene wear assessment in total knee replacement. In *Proceedings of the 19th Annual International Conference of the IEEE Engineering in Medicine and Biology Society.'Magnificent Milestones and Emerging Opportunities in Medical Engineering'(Cat. No. 97CH36136)*, volume 4, pages 1849–1852. IEEE.

Fukuoka, Y., Hoshino, A., and Ishida, A. (1999). A simple radiographic measurement method for polyethylene wear in total knee arthroplasty. *IEEE transactions on rehabilitation engineering*, 7(2):228–233.

Gromov, K., Korchi, M., Thomsen, M. G., Husted, H., and Troelsen, A. (2014). What is the optimal alignment of the tibial and femoral components in knee arthroplasty? *Acta Orthopaedica*, 85(5):480–487. PMID: 25036719.

Hoff, W. A., Komistek, R. D., Dennis, D. A., Gabriel, S. M., and Walker, S. A. (1998). Three-dimensional determination of femoral-tibial contact positions under in vivo conditions using fluoroscopy. *Clinical Biomechanics*, 13(7):455–472.

Hoff, W. A., Komistek, R. D., Dennis, D. A., Walker, S., Northcut, E., and Spargo, K. (1996). Pose estimation of artificial knee implants in fluoroscopy images using a template matching technique. In *Proceedings Third IEEE Workshop on Applications of Computer Vision. WACV'96*, pages 181–186. IEEE.

Hunter, D. J. and Bierma-Zeinstra, S. (2019). Osteoarthritis. *The Lancet*, 393(10182):1745 – 1759.

Kappel, A., Laursen, M., Nielsen, P. T., and Odgaard, A. (2019). Relationship between outcome scores and knee laxity following total knee arthroplasty: a systematic review. *Acta orthopaedica*, 90(1):46–52.

Kaptein, B., Valstar, E., Stoel, B., Rozing, P., and Reiber, J. (2003). A new model-based rsa method validated using cad models and models from reversed engineering. *Journal of biomechanics*, 36(6):873–882.

Kasten, Y., Doktofsky, D., and Kovler, I. (2020). End-to-end convolutional neural network for 3d reconstruction of knee bones from bi-planar x-ray images. *arXiv preprint arXiv:2004.00871*.

Kim, H., Lee, K., Lee, D., and Baek, N. (2019). 3d reconstruction of leg bones from x-ray images using cnn-based feature analysis. In *2019 International Conference on Information and Communication Technology Convergence (ICTC)*, pages 669–672. IEEE.

Kulkongkoon, T., Cooharojananone, N., and Lipikorn, R. (2018). Knee implant orientation estimation for x-ray images using multiscale dual filter and linear regression model. In Meesad, P., Sodsee, S., and Unger, H., editors, *Recent Advances in Information and Communication Technology 2017*, pages 140–149, Cham. Springer International Publishing.

Markelj, P., Tomaževič, D., Likar, B., and Pernuš, F. (2012). A review of 3d/2d registration methods for image-guided interventions. *Medical image analysis*, 16(3):642–661.

Meneghini, R. M., Mont, M. A., Backstein, D. B., Bourne, R. B., Dennis, D. A., and Scuderi, G. R. (2015). Development of a modern knee society radiographic evaluation system and methodology for total knee arthroplasty. *The Journal of Arthroplasty*, 30(12):2311 – 2314.

Price, A. J., Alvand, A., Troelsen, A., Katz, J. N., Hooper, G., Gray, A., Carr, A., and Beard, D. (2018). Knee replacement. *The Lancet*, 392(10158):1672 – 1682.

Toft, P. (1996). *The Radon Transform - Theory and Implementation*. PhD thesis.

Walker, S. A., Hoff, W., Komistek, R., and Dennis, D. (1996). " in vivo" pose estimation of artificial knee implants using computer vision. *Biomedical sciences instrumentation*, 32:143–150.

Zuffi, S., Leardini, A., Catani, F., Fantozzi, S., and Cappello, A. (1999). A model-based method for the reconstruction of total knee replacement kinematics. *IEEE Transactions on Medical Imaging*, 18(10):981–991.